# Optical fiber probe for biomedical Raman spectroscopy

Jason T. Motz, Martin Hunter, Luis H. Galindo, Joseph A. Gardecki, John R. Kramer, Ramachandra R. Dasari, and Michael S. Feld

*In vitro* experiments have demonstrated the ability of Raman spectroscopy to diagnose a wide variety of diseases. Recent *in vivo* investigations performed with optical fiber probes were promising but generally limited to easily accessible organs, often requiring relatively long collection times. We have implemented an optical design strategy to utilize system throughput fully by characterizing the Raman distribution from tissue. This scheme optimizes collection efficiency, minimizes noise, and has resulted in small-diameter, highly efficient Raman probes that are capable of collecting high-quality data in 1 s. Performance has been tested through simulations and experiments with tissue models and several *in vitro* tissue types, demonstrating that this new design can advance Raman spectroscopy as a clinically practical technique. 

*OCIS codes:* 120.3890, 170.5660, 120.4570, 060.2310.

## 1. Introduction

Raman spectroscopy is proving to be a valuable and accurate tool for diagnosing disease and studying biological tissue.[1,2] This technique utilizes inelastically scattered laser light to provide detailed information about vibrations of molecular bonds. Because each chemical moiety in a sample has a unique molecular structure, its composition can be evaluated through analysis of the generated Raman spectrum.

*In vitro* studies have established the medical potential of Raman spectroscopy.[3–6] In fact, many diseases have been investigated because Raman spectroscopy has the ability to provide specific information about a wide variety of chemical and morphological constituents that cannot be obtained with other methods. For example, the rupture of unstable atherosclerotic plaque in coronary arteries accounts for the majority of fatal myocardial infarctions. It has been established that the likelihood for a plaque to rupture is related to its chemical composition.[7,8] Raman spectroscopy may have a unique ability to differentiate the most unstable lesions on the basis of their composition. If this method could be successfully implemented clinically with real-time analysis, it could be used for a range of applications such as diagnosing cardiovascular disease and guiding effective therapy, and characterizing malignant tumors and ensuring their complete resection by monitoring surgical margins.

Many medical applications require remote sampling by use of optical fibers in which the sizes of the probe and the fiber bundle are strictly limited by anatomic considerations. For example, the ability to clinically evaluate coronary atherosclerosis and breast cancer requires probes that are ~2 mm or less in diameter so they can be incorporated into standard cardiovascular catheters or configured for optical needle biopsy. Similar constraints are presented with endoscopic applications, in which the probe must be inserted into a narrow-diameter channel. In addition, data acquisition time must be limited to a few seconds at most.

There have been substantial advances in optical fiber probe designs over the past decade, indicating that Raman spectroscopy is a potentially useful clinical technique. Low-OH fused silica has been determined as the optimal fiber substrate for use in the near infrared.[9] The necessity for designing proper optical filters to remove the probe background has been established,[10] and numerous probe configurations have been explored.[11–14]

Recently there have been reports of *in vivo*

The authors are with the George R. Harrison Spectroscopy Laboratory, Massachusetts Institute of Technology, Cambridge, Massachusetts 02139. M. S. Feld's e-mail address is msfeld@mit.edu.

Received 27 May 2003; revised manuscript received 29 September 2003; accepted 22 October 2003.

0003-6935/04/030542-13$15.00/0

investigations,[15–24] many of which used commercially available probes. The majority of these studies have been confined to skin and other easily accessible organs.[16–19,22–24] Those that provided access to more-remote sites required undesirably long collection times for practical clinical use because the excitation wavelengths and optical configurations that were used were not optimized for studying tissue.[15,20,21] Thus a key impediment to attaining the clinical potential of Raman spectroscopy is a lack of small-diameter optical fiber Raman probes with suitable optical filters that are capable of delivering excitation laser light to *in vivo* tissue and of efficiently collecting the Raman scattered light.

The design goals for the Raman probes described in this paper are, therefore, as follows: The probes must be small (~2 mm) and flexible for access to remote organs. They must be able to collect high signal-to-noise ratio (SNR) spectra in approximately 1 s for accurate clinical application of the spectral models used for analysis. This must be done with safe levels of laser exposure and be accomplished by minimizing all sources of noise while maximizing throughput and efficiency.

There are several sources of noise that can be minimized. Detector dark charge and read noise are reduced by use of cryogenically cooled charge-coupled device (CCD) detectors. The choice of excitation wavelength also influences the SNR. We have found that 785-nm excitation, as is done with many Raman probe designs, results in at least a fourfold increase in tissue fluorescence than 830-nm excitation. This increased fluorescence adds significant shot noise to the data. Although longer excitation wavelengths further reduce tissue fluorescence, the Raman cross sections are simultaneously reduced because they depend approximately on the excitation frequency to the fourth power.[25] Furthermore, the absorption coefficient of water rapidly increases at longer wavelengths, thereby decreasing penetration depth and attenuating the signal. Excitation wavelengths greater than 830 nm also prohibit the use of CCD detectors, thereby compromising the ability to collect an entire Raman spectrum with a single exposure.

A major source of noise specific to optical fiber Raman probes is the long-recognized problem of spectral background generated in the delivery and collection fibers themselves. This background is orders of magnitude larger than the signal from the tissue site that is being examined. It is composed of Raman light from the fused-silica core, fluorescence from impurities and dopants used to produce fibers of a particular numerical aperture (NA), and signal from various jacket materials. Laser light in the delivery fibers generates an intense fiber background caused by the long path length, typically 3–4 m, traversed in the fibers. This fiber spectrum is scattered from the tissue's surface and gathered, along with the tissue's Raman spectrum, by the collection fibers. The background often masks the tissue's Raman signal, which is generated from only ~1 mm of sample owing to the relatively short penetration of light into tissue. Laser light backscattered from the tissue also enters the collection fibers, producing additional fiber background and further compromising the quality of the tissue's spectrum reaching the detector. In addition to obscuring and distorting the spectrum of interest, the intense fiber background adds shot noise to the signal. This noise is often larger than the tissue's Raman bands, and it is therefore necessary to remove as much of the background as possible by using optical filters.

The other consideration in probe design, optimizing throughput and maximizing collection efficiency, has two components. The first has to do with the inherently weak nature of the Raman effect. Approximately only 1 of $10^9$ excitation photons that reach the tissue will be converted into a Raman photon. It is therefore crucial to design a high-throughput optical system to collect signals with sufficient SNR for accurate analysis in a clinically realistic time frame. The second component is concerned with the optical characteristics of the tissue itself. The signal of interest is directly attenuated by absorbance of the excitation laser and the generated Raman light. Furthermore, collection of the Raman light is confounded by light scattering, which causes the photons to be widely diffused over large areas and angles. Thus the simple probe designs used for other types of spectroscopy, or for studying nonturbid samples, are not ideal for this application. Because of these difficulties and the small size constraints, this is a problem in micro-optical design that requires understanding the optical properties of the target sample.

To achieve our design goals we developed an optical fiber Raman probe that (1) removes a majority of the optical fiber background, (2) employs 830-nm excitation, (3) maximizes signal collection from the Raman source generated in the tissue, allowing data collection to be completed in a few seconds or less, and (4) operates at safe fluence levels while (5) limiting the size of the rigid distal tip to less than a few millimeters in length and ~2 mm in diameter.

The remainder of this paper is organized as follows: First, the design process employed in constructing the Raman probes, including the use of optical filters to remove fiber background, general considerations for optical system design, and specific methods for working with highly scattering samples, is elucidated. This is followed by a detailed description of construction of the Raman probe. The probe's performance is then demonstrated in independent sections through simulations and experimental tests. Finally, a discussion and a critique of the current Raman probe design, along with prospects for future design modifications, are presented.

## 2. Raman Probe Design Strategy

### A. Optical Filters

A simple analysis indicates that detected fiber spectral background is produced equally in both excitation and collection fibers.[26] Therefore, as has been

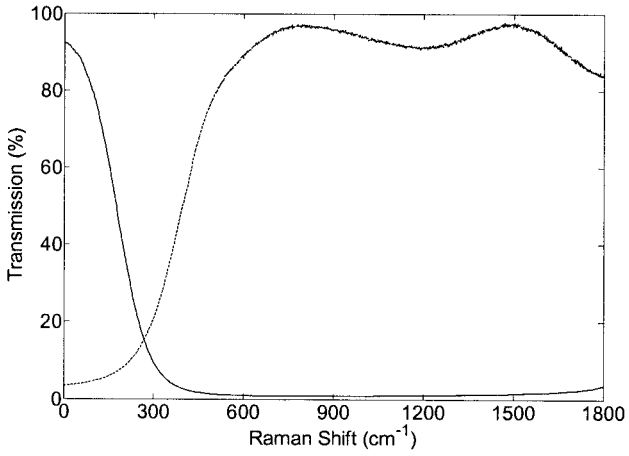


Fig. 1. Transmission of the long-pass filter (peaked beyond 500 cm$^{-1}$) for collection and the short-pass filter (peaked at 0 cm) for excitation, used in the Raman probe filter module, where 0 cm$^{-1}$ = 830 nm.

noted by other investigators,[10] two different filters are required at the distal end of the probe to suppress the unwanted signal: one for delivery and one for collection. Delivery fibers must be terminated with a short-wavelength-pass or a bandpass filter that transmits the laser excitation light while blocking the longer-wavelength spectral background from the fibers. The collection fibers must be preceded by a long wavelength-pass filter or notch filter, which transmits the tissue's Raman spectrum while blocking laser light backscattered from the tissue. The filters must perform these functions over the range of angles that corresponds to the NAs of the fibers that the filters serve.

To accommodate the filters in the distal end of the probe we designed a novel filter module. This module consists of a rod carrying a short-pass dielectric filter coating on one plane face, fitted into a tube carrying a long-pass dielectric coating, also on one plane face. We use rods and tubes that are made from either sapphire or fused silica that are separately coated with their respective filters before assembly (dielectric-stack filters deposited by Research Electro-Optics, Inc., Boulder, Colo.). The rod is wrapped with a thin sheet of metal to prevent cross talk by providing optical isolation between the components. The module is placed at the distal end of the probe between the fiber bundle and the collection optics. Typical filter performance curves used in the Raman probe are shown in Fig. 1 (0 cm$^{-1}$ = 830 nm). Peak transmissions are typically >90%, whereas rejection of the unwanted light is >96%.

### B. General Considerations of Optical System Design

In general, the throughput ($\Theta$, or *étendue*) of an optical system is given by the product of its collection area ($A$) and its projected solid angle ($\Omega'$), where

$$\Omega' = \pi \sin^2(\theta) \qquad (1)$$

is evaluated for the half-angle ($\theta$) of collection, measured with respect to the optical axis.[26,27] If one neglects fiber coupling limitations along with reflection and transmission losses of all optical components, factors that are easily optimized, the system's collection ability is limited by the throughput of its most restrictive element. The design goal is to conserve this quantity throughout the system.

In ideal spectroscopy systems throughput is determined by the spectrograph–CCD detection equipment. Our current spectrograph has a NA of 0.278 (Holospec $f$/1.8i; Kaiser Optical Systems, Inc., Ann Arbor, Mich.), such that $\Omega_D' = 0.225$ sr. The entrance slit's height is 8 mm. This spectrograph is coupled to a back-illuminated, deep depletion CCD detector (Spec-10: 400BR, Roper Scientific, Trenton, N.J.) that also has a height of 8 mm and does not, therefore, compromise throughput. To achieve sufficient spectral resolution (~8 cm$^{-1}$) for biological Raman spectroscopy we utilize a 0.2-mm slit width at the entrance to the spectrograph. Thus our maximal area of collection, $A_D = 1.6$ mm$^2$, results in a theoretical maximal throughput of $\Theta = A_D\Omega_D' = 0.360$ mm$^2$ sr for the detection system. Detection of light from a Raman source is limited by this product, and collection optics are designed to conserve system throughput.

Diffuse scattering in the tissue results in emission of the Raman light over a large area and solid angle, each with a particular distribution. Optimizing signal collection from such a source requires two steps. First, the distribution of the Raman light emerging from the turbid medium must be determined. This distribution defines the potential light-collection efficiency for the given Raman source, within the throughput constraints, as the area (or angle) of collection is varied. The system constant determined by the spectrograph is related to the collection optics through $\Theta = A_c(r_c)\Omega_c'(\theta_c)$. This equation defines a unique relationship between the radius, $r_c$, and the angle, $\theta_c$, of collection. These two parameters cannot be independently selected: If one quantity is increased, the other must be correspondingly reduced. Hence these properties are used to determine the optimal trade-off between collection solid angle $\Omega_c'(\theta_c)$ and area $A_c(r_c)$ to maximize efficiency for design of the collection optics to be utilized with the particular Raman source.

The optics in the distal end of an optical fiber probe must also be designed to transform the Raman scattered light for efficient coupling into the collection fibers, which should be chosen to have the same NA as the spectrograph (assuming a 1:1 imaging system). Furthermore, to optimize signal collection it is necessary to maximize the cross-sectional area of the collection fibers in the distal probe tip. This is achieved by use of a single central excitation fiber, surrounded by as many closely packed rings of collection fibers as possible, up to what can be accommodated by the spectrograph–CCD combination and incorporated into the probe diameter. The circular bundles of fibers in the distal end are then reshaped

at the proximal end into a linear array for coupling to the spectrograph.

Proper choice of excitation optics is also crucial. The intensity of the background generated in the fused-silica optical fibers is proportional to the square of the NA but is relatively independent of the core diameter.[28] Therefore, whereas it is desirable to match the collection fiber's NA to the spectrograph, it is preferable to use an excitation fiber with a lower NA. Reducing this NA also provides decreased beam divergence at the distal end, thereby improving the short-pass filter's performance. However, studies in our laboratory have indicated that fibers with very low NAs (0.12) exhibit substantially increased broadband fiber background, presumably generated from doping materials used in the cladding. Thus we have found that using a moderate NA (0.22) is most effective. One can then choose the appropriate excitation fiber diameter to ensure safe illumination fluence at the tissue while limiting the spot size to facilitate efficient collection.

### C. Characterization of the Raman Source

Determination of optimal collection geometry requires characterization of the distribution of Raman light from the tissue. This source has a given brightness $B(r, \theta)$ [W cm$^{-2}$ sr$^{-1}$] emerging from the sample that is a function of the radial distance ($r$) from the excitation source on the optical axis of the system and of the emission angle ($\theta$) from the surface normal. The total power of Raman scattered light available for collection from the tissue is given by

$$P_{\text{Raman}} = \iint_{A_S \Omega_S} B(r, \theta) \mathrm{d}A \mathrm{d}\Omega, \tag{2}$$

where $\mathrm{d}A = (2\pi r)\mathrm{d}r$ and $\mathrm{d}\Omega = 2\pi \sin(\theta)\mathrm{d}\theta$. The integrals are carried over the entire area, $A_s$ ($0 < r < \infty$), and solid angle, $\Omega_s$ ($0 < \theta < \pi/2$), of the source, the latter of which is limited to $2\pi$ for backscattering geometries.[29]

If it is assumed that $B(r, \theta)$ is separable, $B(r, \theta) = \beta_1(r)\beta_2(\theta)$, then the radial and angular contributions can be more easily measured experimentally. These independent distributions are used to approximate the light emitted from the source that is potentially available for collection such that

$$P_{\text{Raman}} \approx \int_{A_S} \beta_1(r)\mathrm{d}A \int_{\Omega_S} \beta_2(\theta)\mathrm{d}\Omega = P_r P_\theta, \tag{3}$$

where $P_r$ and $P_\theta$ are the integrated radial and angular distributions, respectively, emanating from the tissue.

The total collection efficiency of the optical system [$\eta_T(r_c, \theta_c)$] for this Raman source is calculated by integration of the radial and angular brightness over the properties of the collection optics, normalized by the total light emitted from the source and constrained by throughput conservation. The resultant efficiency curve,

$$\begin{aligned}\eta_T(r_c, \theta_c) &\approx \eta_1(r_c)\eta_2(\theta_c) \\ &= \frac{\int_{r=0}^{r_c} r\beta_1(r)\mathrm{d}r}{\int_{r=0}^{\infty} r\beta_1(r)\mathrm{d}r} \frac{\int_{\theta=0}^{\theta_c} \sin(\theta)\beta_2(\theta)\mathrm{d}\theta}{\int_{\theta=0}^{\pi/2} \sin(\theta)\beta_2(\theta)\mathrm{d}\theta},\end{aligned} \tag{4}$$

is used to guide design of the probe optics by specifying the optimal trade-off between collection radius and solid angle. Angular efficiency $\eta_2(\theta_c)$ can be transformed into a function of radius $\eta_2[r_c(\theta_c)]$ by use of the relationship between angle and radius established by throughput conservation, resulting in a single variable function $\eta_T(r_c)$ for the total collection efficiency.

Guided by our desired instrumental application for diagnosing atherosclerosis, we examined the radial and angular distributions of Raman light from arterial tissue. For convenience we assumed $B(r, \theta)$ to be separable, an approximation that should not introduce significant error. Normal arterial tissue was used because it typically exhibits the weakest signal compared with other arterial disease states, because of its optical properties (e.g., scattering and absorption coefficients) and relative Raman cross sections.

Experimental characterization of the spatial distribution $\beta_1(r)$ of Raman light was determined from a modification of the system described by Koo for analysis of blood analytes.[29] Briefly, 830-nm excitation was focused and directed to the sample via a small prism. The excitation spot diameter was ~100 μm, and the sample was held in a quartz cuvette containing phosphate-buffered saline (pH = 7.4). The backscattered light was collected by a Cassegrain objective with an angular range of 14°–33°. This entire range of Raman light was collected, collimated, and notch filtered to reject the Rayleigh scattered light, and the image was focused to a 1.7-mm-diameter spot in the image plane. A single 100-μm-core optical fiber was translated laterally across the image of the tissue with a step size of 250 μm to collect discrete spatial regions of Raman light emitted from the tissue. When the magnification from the objective is taken into account, this step size value corresponds to a step size of ~104 μm at the sample surface. The fiber was coupled into an $f/1.8$ spectrograph, and the light was dispersed onto a CCD detector. The intensity of the 1450-cm$^{-1}$ Raman band from—$CH_2$ bending modes was integrated, normalized to the maximum signal, and plotted as a function of radial distance from the excitation source on the optical axis. The results on the two sides of the excitation beam were nearly symmetrical, and the average $\beta_1(r)$ for the two sides is presented in Fig. 2(a) (circles).

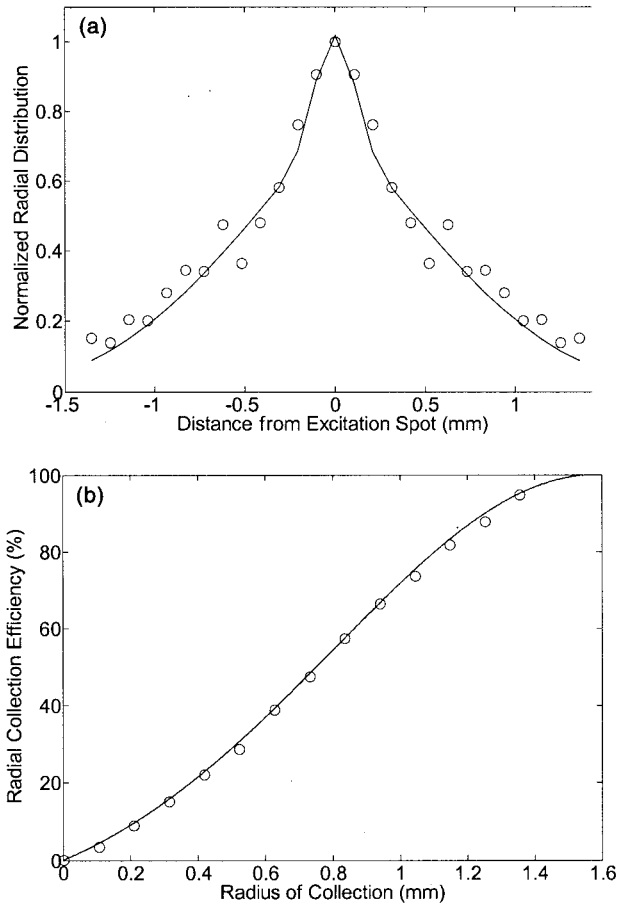


Fig. 2. Spatial distribution of Raman light emitted from normal aorta. (a) Measured (circles) discrete radial distribution $\beta_1(r)$ and a multi-Gaussian fit (solid curve) to the data shown as functions of distance from the excitation beam. The radial collection efficiency [$\eta_1(r_c)$, circles] is plotted in (b) along with a least-squares fit (solid curve) demonstrating a Gaussian profile.

This radial distribution was optimally fitted with a multi-Gaussian [Fig. 2(a), curve], resulting in

$$\beta_1(r) = 0.348 \exp(-r^2/0.025) + 0.113 \exp(-r^2/0.200) + 0.557 \exp(-r^2), \quad (5)$$

with $r$ given in millimeters. It is likely that the narrow distribution represented by the first term is related to Raman light generated by the unscattered component of laser light, producing the most intense Raman energy distribution. The other terms account for diffused light that is also influenced by the layered structure of arterial tissue. These data are then integrated and normalized to yield the radial collection efficiency $\eta_1(r_c)$, shown in Fig. 2(b) as a function of distance from the excitation beam (circles), along with a least-squares fit demonstrating a Gaussian dependence (solid curve).

The angular distribution was determined with a slight modification of the open-air optics Raman system described by Hanlon *et al.*[1] In this case it is much simpler to measure $P_\theta$ directly than to measure the discrete angular distribution $\beta_2(\theta)$. Briefly, 830-nm excitation light was incident normally upon the tissue via a small mirror between the collection lens and the sample. The backscattered Raman light was collected by an $f/1.2$ camera lens (50-mm focal length), which collimated the beam before the beam was notch filtered and then focused onto an $f/4$ spectrograph via an $f/$number-matched lens for detection by a CCD detector. The excitation light was focused down to ~100-μm diameter, and the collection diameter was ~1 mm. The collection lens was preceded by an aperture-stop iris, allowing for variation of the collection angle and direct measurement of the integrated angular Raman distribution. Figure 3 plots the experimentally determined $\eta_2(\theta_c)$ of Raman light from tissue (circles). The distribution plateaus near 20° because of the limited angles collected by the lens. Light emerging from tissue generally follows a $\cos(\theta)$, or Lambertian, dependence, where $\theta$ is the angle with respect to the surface normal. The integrated distribution should therefore have a $\sin^2(\theta)$ dependence, which is also plotted in Fig. 3, demonstrating reasonably good agreement between experiment and theory over the range of angles collected. We shall assume that this agreement holds for angles up to 90°, and remaining analyses will use this full range.

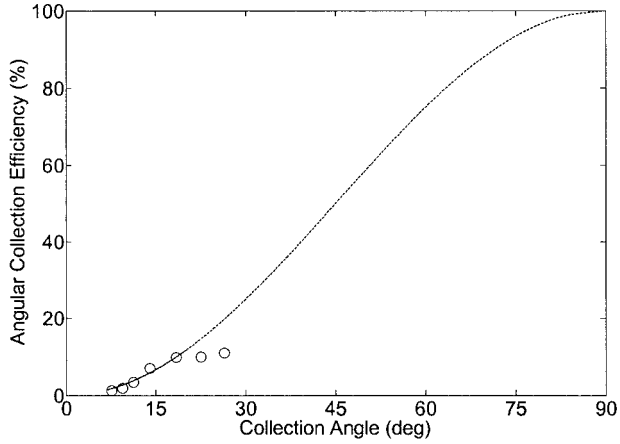


Fig. 3. Integrated angular distribution [$\eta_2(\theta_c)$, circles] and the theoretical $\sin^2(\theta)$ distribution for a Lambertian source (solid curve). Theory and experiment agree well for the range of angles measured, which was limited to 20° by the collection optics. The dotted curve extends the theoretical curve to 90°.

Taking the product of $\eta_1(r_c)$ and the transformed $\eta_2(\theta_c) \rightarrow \eta_2[r_c(\theta_c)]$ from Figs. 2(b) and 3 results in the efficiency curve $\eta_T(r_c)$ (Fig. 4, thicker solid curve) for this combination of system throughput and tissue. Optimal efficiency of 8.6% occurs at a collection radius of 0.19 mm and corresponding 90° angle. Smaller radii of collection result in imaginary collection angles owing to throughput conservation, as demonstrated by the saturation of the angular-efficiency (dashed) curve in Fig. 4. This indicates that it is preferable to collect the full angular range of

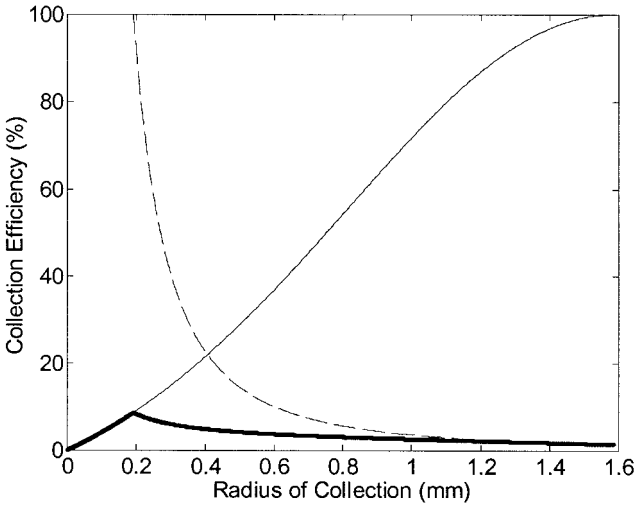


Fig. 4. Angular (dashed curve) and radial (thinner solid curve) collection efficiencies from Figs. 2(b) and 3 as a function of collection radius. The product is the total collection efficiency $\eta_T(r_c)$ (thicker solid curve).

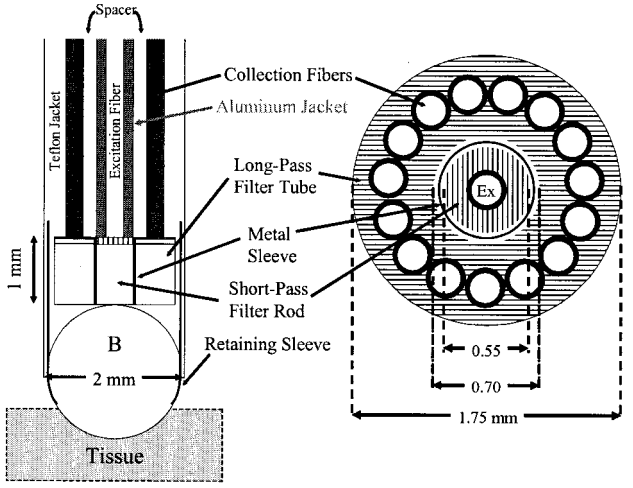


Fig. 5. Schematic of the Raman probe tip, showing a longitudinal view at the left and a transverse cross section at the fiber–filter interface at the right (see text for details). Ball lens B is in contact with the filter module that couples to the fiber bundle.

Raman light from the most intense area of illumination rather than to collect a lower range of angles while extending the collection to the weaker tails in the edge of the distribution.

### D. Raman Probe Configuration: Technical Implementation

We then incorporated the results of the Raman source characterization studies into an optical design code (Zemax v. 10.0; Focus Software, Inc., Tucson, Ariz.) to determine appropriate optics for maximal signal collection and transformation of the gathered light for efficient coupling into the optical fibers. Although it is possible to design sophisticated optics to perform close to these specific parameters, the spatial constraints imposed by the given application would make construction prohibitively difficult. In fact, investigations with Zemax indicate that the use of a simple ball lens with a large refractive index results in reasonable performance. Several substrates were investigated, and we found most high-refractive-index glasses to be extremely fluorescent because of the doping materials that were used. However, sapphire, whose refractive index is 1.77, allows for wide-angle collection. Sapphire exhibits no fluorescence, has only a single, sharp Raman band in our region of interest, and is optically clear throughout a broad wavelength region. In addition, sapphire is extremely hard, thus making it an excellent choice for use in a multiple-use Raman probe.

The resultant Raman probe design is presented in Fig. 5. The left-hand side shows a longitudinal view of the probe tip, and the right-hand side shows a cross-sectional view at the level of the fiber–filter interface. There is a central excitation fiber (Fiberguide Industries, Stirling, N.J.) with an aluminum jacket for optical isolation to prevent cross talk with the collection fibers. This fiber is placed in alignment with the short-pass excitation rod, shown as vertical hatchings. The rod is placed inside the long-pass collection filter tube; the two are optically isolated by a metal sleeve (Pd; Surepure Chemetals, Florham Park, N.J.). The excitation fiber is then buffered out to ensure proper alignment of the 15 collection fibers, which are aligned with the center of the long-pass filter tube shown by horizontal hatchings. The central excitation fiber has a 200-$\mu$m core with a 0.22 NA. The collection fibers (Fiberguide Industries, Stirling, N.J.) also have a 200-$\mu$m core but have a 0.27 NA, which is closely matched to that of the spectrograph. The filters are secured to the fibers with an index-matching optical cement ($Na_2Si_3O_7$; Sigma-Aldrich, St. Louis, Mo.) and the entire fiber bundle–filter module is encased with black Teflon for binding and protection. The probe length is 4 m.

The filter rod and tube are 1 mm in length, ensuring proper spatial placement of the sapphire ball lens. This geometry addresses two considerations. First, at this fiber–lens separation the excitation light is roughly collimated and is not focused to a tight spot on the tissue, thereby reducing the density of the energy incident upon the sample and preventing possible damage. Second, excellent coupling of the Raman scattered light into the collection fibers is ensured because the ball lens transforms the large angular distribution emerging from the tissue into a beam that falls within the collection fiber's NA. The ball lens is secured into a crimped stainless-steel tube with epoxy (M-31CL; Loctite, Rocky Hill, Conn.), which ensures that no fluid leaks into the tip. The stainless-steel tube is then affixed to the fiber-bundle–filter assembly. To maximize the ball lens's collection efficiency, we used no adherents on the inner surface.

The total diameter of this probe is less than 3 mm.

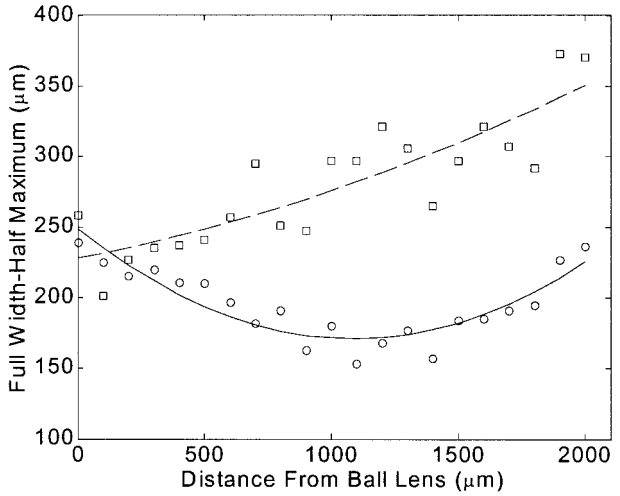


Fig. 6. Results of simulation of the Raman probe excitation spot diameter. Slight focusing occurs 1 mm from the ball lens with no scattering (circles with solid curve), but an immediate divergence occurs when the probe is in contact with a scattering medium (squares with dashed curve). The curves represent least-squares fits with a second-order polynomial.

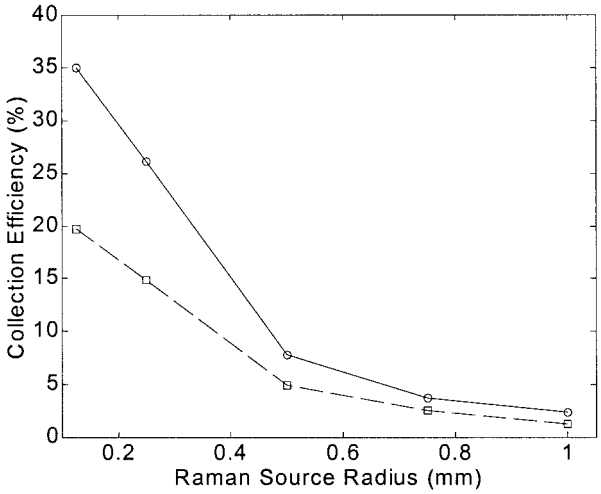


Fig. 7. Simulated Raman probe collection efficiency as a function of Raman source radius, showing significant increases with smaller sources. Results with the probe–sample interface in air (circles with solid curve) are ~1.75 times greater than that with a scattering medium (squares with dashed curve).

The current size-limiting factor is the diameter of the ball lens, which is 2 mm to accommodate the entire width of the filter tube. This filter size was chosen because we also used this geometry to construct Raman probes with two rings of collection fibers (a total of 27 fibers), which more fully utilize the spectrograph throughput. In practice we generally use a single ring of collection fibers because it provides excellent signal collection and is much more flexible and easier to construct. Recent studies have shown that the probe diameter can be reduced without significantly degrading collection efficiency. The diameter of the central collection rod was chosen for ease of construction to be 0.55 mm. All components of the probe are constructed of medical-grade materials that can withstand standard cold gas ethylene oxide sterilization for surgical procedures.

### 3. Probe Performance: Simulation Results

The Raman probe design was tested through simulations during the design phase and experimentally after construction. We performed the simulated experiments discussed in this section with a Zemax model of the probe to investigate two aspects of the probe design. First, the area of the excitation light spot delivered to the tissue was investigated to ensure safety. Second, we examined collection efficiencies for various Raman sources to determine probe performance over a range of conditions.

Results of simulations of the excitation spot diameter are shown in Fig. 6. Two configurations were investigated, one with the probe placed in air (circles) and one with the probe submerged in a simulated tissue model (squares); the latter was the more likely clinical geometry. Second-order polynomial fits to the simulated data are also plotted to characterize the irradiance. The tissue model was constructed with the index of refraction of water and scattering properties similar to those reported in the literature for arterial tissue: $g = 0.9$; mean-free path, 0.27 mm.[30] As can be seen from the figure, when the probe is in air there is a slight focusing to a FWHM of ~175 μm approximately 1 mm away from the lens. However, in the scattering case the beam begins to diverge immediately from the surface of the ball lens, never falling below a FWHM of <200 μm. This spot diameter will produce fluences well below any reported damage thresholds with laser powers and exposure times that would be used in a clinical setting. In fact, our data collection protocols are designed to use ~100-mW excitation for times of <5 s, thus producing fluences much below those reported in the literature.[17]

Collection efficiencies were determined from the Zemax model in a similar way (Fig. 7). Lambertian sources of various radii and a spatially top-hat distribution were placed in contact with the probe, and the percentage of light emerging from the proximal end of the 0.27-NA collection fibers was measured. For these simulations, a model of our dual-ring probe with 27 collection fibers was implemented because this more fully utilizes the spectrograph throughput. Again, two situations were investigated. The first had the source in contact with the probe but the lens maintained in air such that the external surface of the ball lens did not experience any index matching (circles with solid curve). The second also had the source in contact with the probe, but now the lens and the source were both submerged in the simulated tissue model described above (squares with dashed curve). The probe exhibits excellent collection efficiencies (as much as 35%) for small sources in air, but

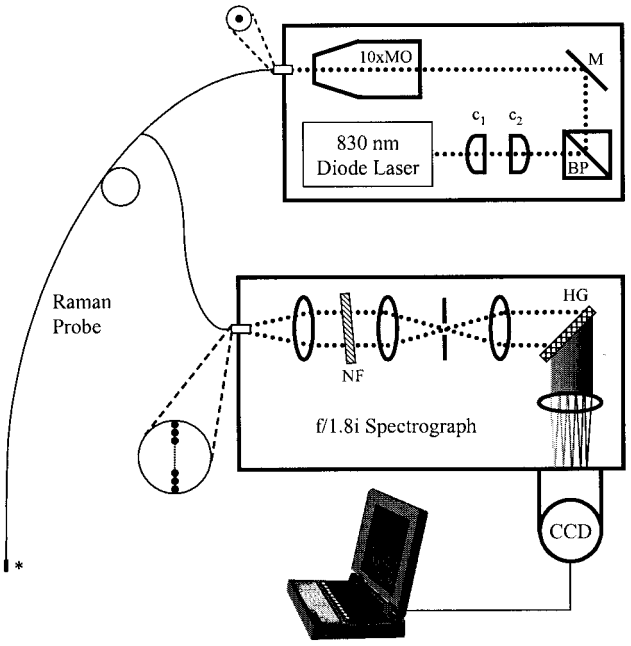


Fig. 8. Schematic of the Raman spectroscopy system used for experimental testing of the Raman probe (see text for details). Details of the probe tip are presented in Fig. 5. 10 × MO, MO, microscopic objective.

the efficiency falls off as the source radius increases. The tissue model results are also excellent, producing efficiencies ~57% as large as those when the probe is not index matched.

An additional configuration was also investigated, wherein the measured Raman distribution from the source (Figs. 2 and 3) was modeled and placed at the end of the probe. This resulted in collection efficiencies of 3.5% and 1.7% for the air and tissue interfaces, respectively. The results of the air interface should be compared with the collection efficiency shown in Fig. 4. The maximal collection efficiency of 8.6% results from fully utilizing the throughput; however the limited packing fraction obtained by use of optical fibers results in a 53% utilization of the spectrograph slit area. Therefore the maximal collection efficiency expected should be 4.6%, showing that the ball lens is performing close to the peak. Multiplying the efficiency curve by the same 53% caused by the reduced throughput indicates a collection radius ($r_c$) of 0.27 mm, which corresponds to a collection angle of 45°. Although there is room for improvement, this is an excellent collection efficiency, and the ease of implementation is highly practical.

## 4. Probe Performance: Experimental Results

### A. Methods

The Raman probe's performance was experimentally tested in three ways. First, we examined various known Raman scatterers to assess filter performance. Second, we developed tissue phantoms to evaluate the effects of scattering and absorption on signal and background collection. Finally, *in vitro* spectra of artery and breast tissue were collected and evaluated with our spectroscopic models.

A schematic of the experimental system used in these investigations is shown in Fig. 8. Light from an 830-nm diode laser (Process Instruments, Salt Lake City, Utah) is collimated by two cylindrical lenses ($c_1$ and $c_2$), directed through a bandpass filter (BP; Kaiser), redirected by a gold-coated mirror (M) and focused onto the Raman probe excitation fiber by a 10× microscope objective (Newport, Irvine, Calif.). The proximal linear array of collection fibers from the Raman probe are input to the $f/1.8$ spectrograph, which collimates the light before it is notch filtered (NF), focused onto a slit, and recollimated for dispersion by the holographic grating (HG). Finally, the dispersed light is focused onto a liquid-nitrogen-cooled, back-illuminated, deep depletion CCD detector, which is interfaced with a laptop computer.

We examined barium sulfate ($BaSO_4$), a well characterized Raman scatterer, to evaluate the probe filtering and collection performance. $BaSO_4$ powder was tightly packed into sample holder with no coverslip. The Raman probe was then placed in light contact with the sample, and spectra were collected for 0.1 s with 100-mW excitation power. The highly reflective nature of packed $BaSO_4$ generally produces an intense fiber background in unfiltered optical fiber probes, making this a useful sample with which to evaluate filter performance.

Tissue phantom studies were designed to mimic the range of scattering and absorption properties of arterial tissue that have been reported in the literature.[30] Samples were prepared with a combination of monodispersed 1.03-μm latex microspheres (Duke Scientific Corporation, Palo Alto, Calif.) for scattering, hemoglobin (Sigma, St. Louis, Mo.) and India ink (Triangle Biomedical Sciences, Durham, N.C.) for absorption, and deionized water. A stock solution of sodium perchlorate ($NaClO_4$) was added to the samples with a constant concentration as the target Raman molecule. Various combinations of the constituents were mixed to produce nine phantoms of constant volume and perchlorate ($ClO_4^-$) concentration with absorption ($\mu_a$) and reduced scattering ($\mu_s'$) coefficients of 1.31, 1.79, and 2.25 $cm^{-1}$ and 22, 29 and 36 $cm^{-1}$, respectively. Concentrations to produce these optical properties were determined with a modified version of the Mie code of Bohren and Huffman.[31]

The phantoms were placed in 2-in. (5.08-cm) deep, 3/4-in. (1.9-cm) wide glass vials, and the probe tip was submerged just under the surface of the liquid for sampling. The sample was continually circulated by a magnetic stir bar to prevent settling of the microspheres. Spectra were collected by use of 100-mW excitation with the dual-ring Raman probe for a total integration time of 10 s. We integrated the 928-$cm^{-1}$ band of $ClO_4^-$ to determine the Raman collection ability of the probe under these various conditions. We assessed the probe background by examining the intensity of the maximum signal collected (~380 $cm^{-1}$). Other methods for assessing

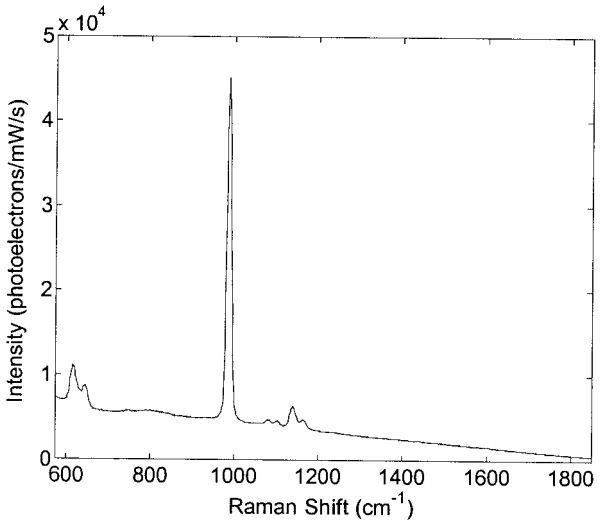


Fig. 9. Raman spectrum of $BaSO_4$ collected with the single-ring probe, demonstrating the efficiency of the filter module. There is minimal evidence of fiber background in this spectrum.

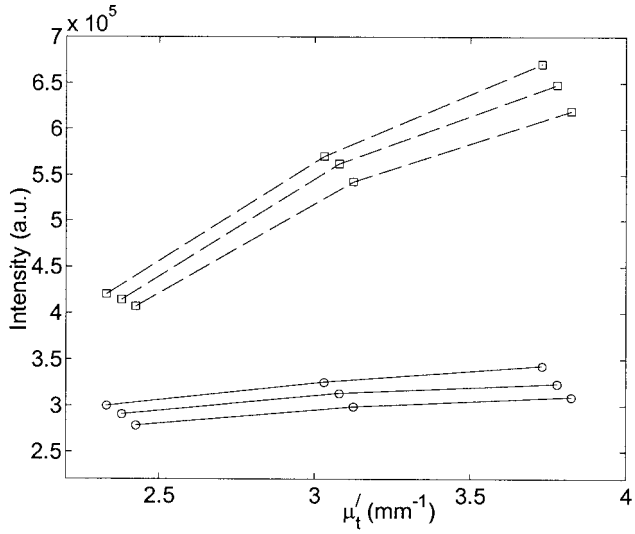


Fig. 10. Results of the tissue phantom studies showing signal collection as a function of the reduced transport coefficient. Intensities of the perchlorate signal of interest (circles and solid curves) are plotted along with the fiber background (squares with dashed curves). Lines connecting points of constant absorption were drawn to demonstrate the effects of signal collection with increased scattering.

background are to integrate over the 800-$cm^{-1}$ Raman band from the quartz background or over the 750-$cm^{-1}$ Raman band produced by the sapphire ball lens. All these methods produced similar results.

Finally, we examined *in vitro* tissue specimens with the single-ring Raman probe, using 100-mW excitation power and collection times ranging from 1 to 60 s. Samples of human aortic tissue were collected post mortem, and breast samples were collected during surgical resection. Samples were snap frozen in liquid nitrogen immediately after being harvested and were stored at −85 °C until the time of examination. Samples were passively warmed to room temperature in a phosphate-buffered saline bath before examination. Spectra were corrected for filter and CCD spectral response by a tungsten white-light source. We removed the remaining fiber background by subtracting the signal collected by directing the excitation light at a roughened aluminum surface. We removed tissue fluorescence by subtracting a 5th-order polynomial, as previously described.[32] Finally, to demonstrate the practical utility of the Raman probe we fitted the spectra with spectroscopic models previously developed in our laboratory. The breast data were fitted with the model of Shafer-Peltier *et al.*,[33] and the artery spectra were fitted with the morphological model of Buschman *et al.*[3,34] Residuals are calculated as the data minus the fit and are shown on the same scale.

### B. Results

For biological tissue spectroscopy we are generally concerned only with Raman features from 600 to 1800 $cm^{-1}$. Figure 9 shows the Raman spectrum of packed $BaSO_4$, a well-characterized Raman scatterer. Unlike liquid samples, which typically generate little detected fiber background because there is minimal backscattering, $BaSO_4$ is highly reflective when it is packed and will generate intense fiber background in an unfiltered probe. This spectrum demonstrates the effectiveness of the filter module and optical isolation of the probe because there are almost no detectable features of the fiber background above 550 $cm^{-1}$, other than a slightly increased sloping background. Even the intense silica band at 800 $cm^{-1}$ is not discernable.

Results of the tissue phantom studies are presented in Fig. 10. The signals from the major perchlorate Raman band at 928 $cm^{-1}$ (circles and solid curves) and from the most intense region of the probe background at ~380 $cm^{-1}$ (squares and dashed curves) are plotted as a function of the reduced transport coefficient, $\mu_t' = \mu_s' + \mu_a$. The lines that connect the data points depict samples that have constant absorption and demonstrate how signal collection increases as scattering increases. Conversely, the collected signal decreases with increasing absorption for a given scattering value. Similar trends are seen in both fiber background and the Raman signal; however, the effects of scattering are more dramatic for the background.

Figure 11 is a comparison of optical fiber probe performance and the traditional laboratory system (previously described[1]) when one is looking at normal aorta, a tissue type that shows little variation from site to site. The laboratory system is an open-air optics configuration, unconstrained by the demands of micro-optics, and has been used to develop many successful Raman spectral models.

Figure 11(a) shows data taken with the open-air optics system (lower spectrum), the single-ring Raman probe (middle spectrum), and a traditional

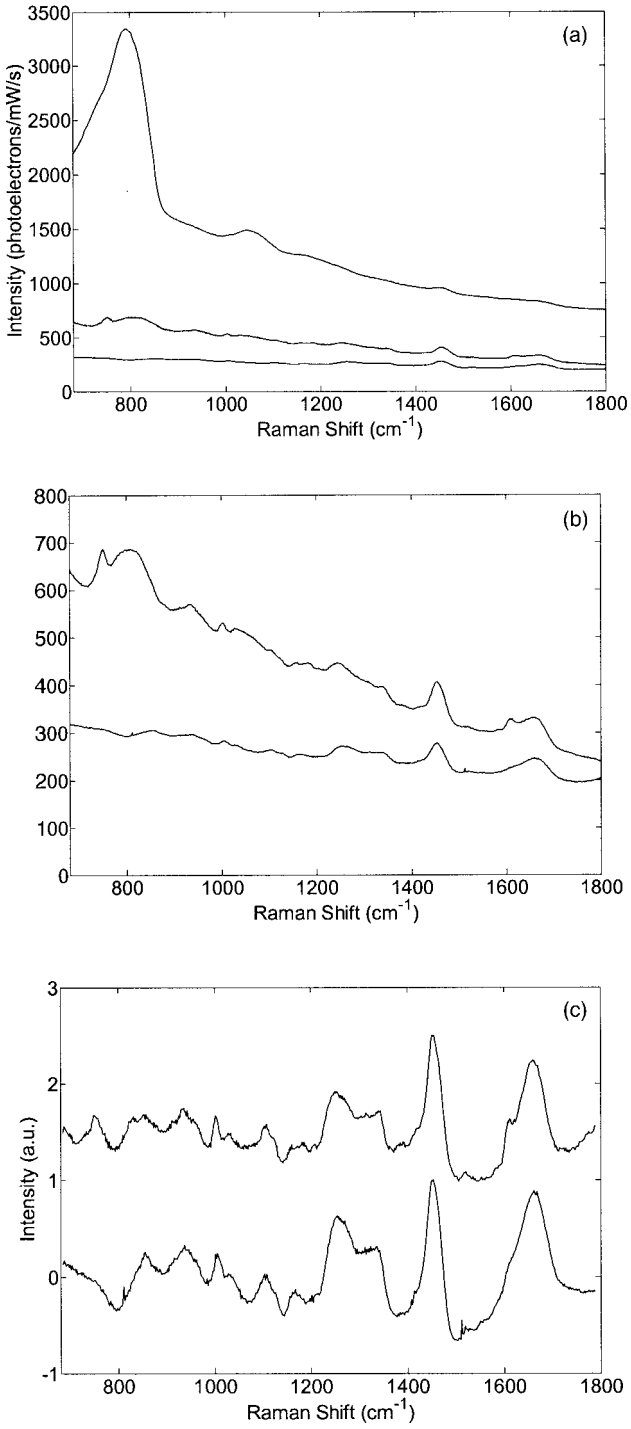


Fig. 11. Comparison of traditional open-air optics Raman system with optical fiber probes. Raw data are shown in (a), demonstrating intense background in an unfiltered probe (upper spectrum) but only a slightly increased background in the Raman probe (middle spectrum) compared with the open-air data (lower spectrum). The slightly increased collection efficiency from the Raman probe (b, upper spectrum) compared with that of the open air optics spectrum (b, lower spectrum) offsets the noise associated with the remaining fiber background. Removal of fiber background from the Raman probe spectrum (c, upper) and tissue fluorescence from the probe and open-air optics (c, lower) data results in identical spectra, except for the peaks at 750 and just below 1600 $cm^{-1}$ that are due to probe tip components.

6-around-1, unfiltered optical fiber probe (upper spectrum), with equivalent excitation powers (100 mW) and collection times (60 s). The data have been corrected for systematic spectral response and CCD detector gain. The intense background and poor collection of the tissue spectrum with the unfiltered probe demonstrate the severity of the problems encountered in Raman probe design.

Figure 11(b) expands the data from the Raman probe and open-air optics system of Fig. 11(a). Although it is difficult to resolve many of the Raman bands over the tissue fluorescence background, observation of the 1450-$cm^{-1}$ band of —$CH_2$ bending, or of the 1004 $cm^{-1}$ band that is due to phenylalanine, indicates slightly increased signal collection from the Raman probe (upper spectrum). There is still some evidence of probe background observed in these data despite the efficient filtering in the Raman probe because, unlike with $BaSO_4$, the Raman signal from tissue is extremely weak. However, Fig. 11(c) shows the results after the fiber background has been subtracted from the Raman probe data, and the tissue fluorescence signal has been removed from both spectra. All spectral features of the fiber background have been accurately removed, and these spectra of normal aorta look nearly identical, other than the peak at 750 $cm^{-1}$ that is due to Raman scattering from the sapphire ball lens, and a small peak just below 1600 $cm^{-1}$ from the epoxy used to secure the lens (upper spectrum). Despite the slightly increased background in the raw data from the Raman probe, on average the two processed spectra have the same SNR because of the increased collection efficiency of the probe. In fact, the dual-ring version of our Raman probe shows greatly enhanced performance over the laboratory system. The intense background in the unfiltered probe prohibits accurate subtraction of the fiber spectrum for comparison with the other data.

Here we have evaluated weakly Raman scattering normal aorta because it is homogeneous. Experiments with tissue types that scatter more than normal aorta suggest that the probe can exhibit even better performance than the laboratory system. However, these differences are difficult to compare directly because of tissue heterogeneity.

Our ultimate goal in designing this new Raman probe is the ability to collect interpretable spectra of tissue in clinically relevant timescales. Figures 12 and 13 show processed spectra collected with the Raman probe in only 1 s with 100-mW excitation. Data are presented as filled circles, with the model fits shown in the overlapping curves and the residuals plotted beneath on the same scale. Figure 12(a) is a spectrum of normal aorta; 12(b), of a noncalcified atherosclerotic plaque; and 12(c), that of a calcified atherosclerotic plaque. Figure 13(a) shows a spectrum of normal breast tissue, and Fig. 13(b) shows that of a malignant breast tumor. Even for the spectra with decreased signal collection, i.e., normal aorta and malignant breast tumors, model fits are excellent and all features that remain in the residual are noise.

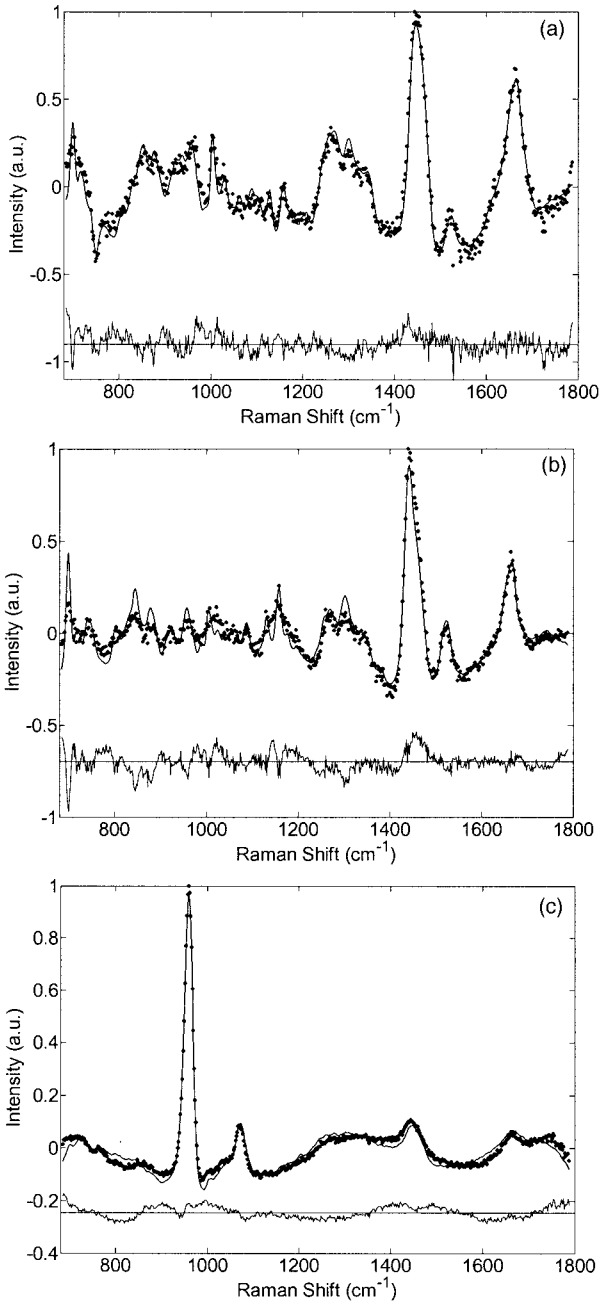


Fig. 12. Raman spectra of (a) normal aorta, (b) noncalcified atherosclerotic plaque, and (c) calcified atherosclerotic plaque. Data are shown as filled circles with the corresponding model fit (solid curves). The residual (data fit) is plotted below on the same scale.

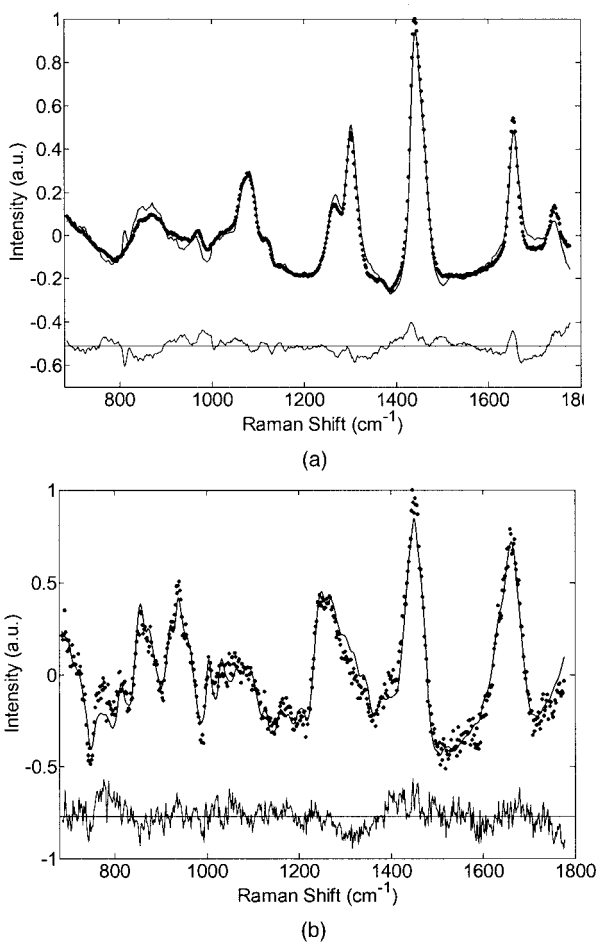


Fig. 13. Raman spectra of (a) normal breast tissue and (b) a malignant breast tumor. Data are shown as filled circles with the corresponding model fit (solid curves). The residual is plotted below on the same scale.

## 5. Discussion

We have outlined a method of optical design for studying biological tissue and demonstrated that this approach results in a Raman probe that is clinically useful in terms of diameter, flexibility, and signal collection. In fact, this optimization approach can be used for optical system design in general, independently of geometrical constraints or tissue types. Koo *et al*. used a similar approach to demonstrate that design of collection optics without the constraints of remote organ access can result in extremely high efficiency, allowing for highly sensitive analytical spectroscopic measurements.[35]

There are two key aspects to this approach: maximizing signal collection and minimizing sources of noise. For optical fiber probes, maximizing signals entails optimizing collection efficiency within the constraints of the spectrograph–CCD detector system. This is done by maximizing the area of the probe available for collection of Raman light and characterizing the Raman source for proper design of collection optics. Minimization of noise also requires several considerations. First, the inherent noise sources from the CCD detector are reduced by use of cryogenically cooled, back-illuminated detectors. Second, the excitation wavelength must be carefully selected to minimize shot noise from tissue fluorescence. For biological samples, 830-nm excitation has proved to be ideal. Finally, in the case of fiber optic probes, as much fiber background as possible must be eliminated to reduce the background's associated shot noise.

The dual-purpose filter module employed in our Raman probe effectively reduces the fiber back-

ground to a level where there is minimal spectral distortion once the remaining background is removed. However, more-efficient filters would further decrease the associated noise and therefore increase the SNR, permitting even shorter collection times. Despite these filter limitations, we have shown that high-quality spectra of several tissue types can be collected in only 1 s by use of excitation powers well below the tissue damage threshold. The fits shown in Figs. 12 and 13 from our spectral models are comparable to those obtained with our traditional laboratory system. The magnitudes of the residuals from these fits are dependent on the intensity of the Raman signal collected from the tissue, and in most cases they are purely noise and show no spectral structure.

Results from the phantom studies show that the probe has decreased collection with increased absorption owing to attenuation of both the excitation and the Raman light. More interestingly, greater signal collection efficiency is observed with increased scattering. This increased signal from highly scattering samples is a result of the Raman source's being confined more closely to the excitation beam, where the ball lens collects most efficiently (Fig. 7). Similar trends for the fiber background are also observed, but the influence of scattering is stronger. Therefore only slight SNR changes are seen for tissues with different scattering and absorption properties if the concentration and cross sections of the Raman scatterers are constant. In addition, further analysis of the background signal, especially from the sapphire ball lens, may result in an internal calibration for scattering and absorption properties of the samples, yielding additional information for disease diagnosis.

One of the limitations of the current probe design is the outer diameter, which is slightly greater than our design goal required for access to coronary arteries. We are currently limited by the size of the filter tube. This filter size was chosen for use with a dual-ring version of the Raman probe. Successful implementation of the single-ring probe has led to further investigations of the possibility of reducing the probe diameter. A smaller diameter means that the number of fibers in the probe must be reduced, thereby reducing the collection area. However, as the number of fibers is reduced, the fibers are also brought closer to the excitation beam where the most intense Raman scattering occurs. Also, reduction of the ball lens's diameter results in greater lens curvature, which leads to increased collection from the more central area of the Raman source. Thus there is an additional efficiency curve, which relates a trade-off between the collection area of the Raman probe and the Raman source's sampling volume. At worst, the collection efficiency will be reduced linearly with the number of fibers. Reducing the number of fibers to a total of nine collection fibers will result in a Raman probe of 1.5-mm total outside diameter and a collection efficiency of 1.2%, which will still produce reasonable SNR for clinical purposes.

This Raman probe has general applicability, and we have shown that it works well for both artery and breast tissues, but it may be advantageous to characterize the particular target tissue for other probe designs to achieve maximum efficiency. The modular nature of the design allows great flexibility with respect to the choice of optics for high-throughput collection such that a variety of optical elements can be used to collect the desired spatial and angular distribution from a target tissue.

Additional front-viewing designs, as well as side-viewing probes for alternative applications, are being pursued. For example, the use of an angled and mirrored half-ball lens, a prism, or a micro-optical paraboloidal mirror will permit efficient radial collection. A tapered tip will permit incorporation of a fiber into needle probes for optical breast biopsies and a slightly smaller diameter will allow breast analysis through ductoscopy for detection of dysplasia. Because of the excellent collection ability of this Raman probe design, other potential uses include skin analysis, transcutaneous monitoring of blood analytes, and evaluation of gastrointestinal cancer.

## 6. Conclusions

We have utilized a quantitative optical design scheme to develop a small-diameter, high-throughput Raman probe that is optimized for use with turbid samples and is able to provide access to remote tissues for spectroscopic evaluation. The probe also uses customized in-line filters at the probe tip to minimize effects of the intense fiber background. High quality spectra of *in vitro* artery and breast tissue with various states of pathology were obtained. These spectra were acquired in only 1 s, demonstrating clinically realistic applicability. Future modifications of the probe will be directed at reducing the diameter and modifying designs for access to other organs to increase the clinical applicability of Raman spectroscopy.

This research was sponsored by the National Institutes of Health (NIH) National Center for Research Resources program (grant P41-RR-02594) and also by NIH grant R01-HL-64675. Support was also generously contributed by the Pfizer Corporation and the Lord Foundation of MIT. The authors thank Tae-Woong Koo for stimulating discussions during the initial design phase and Abigail S. Haka for assistance in collecting the breast data.

## References

1. E. B. Hanlon, R. Manoharan, T.-W. Koo, K. E. Shafer, J. T. Motz, M. Fitzmaurice, J. R. Kramer, I. Itzkan, R. R. Dasari, and M. S. Feld, "Prospects for *in vivo* Raman spectroscopy," Phys. Med. Biol. **45,** R1–R59 (2000).
2. A. Mahadevan-Jansen and R. Richards-Kortum, "Raman spectroscopy for the detection of cancers and precancers," J. Biomed. Opt. **1,** 31–70 (1996).
3. H. P. Buschman, J. T. Motz, G. Deinum, T. J. Römer, M. Fitzmaurice, J. R. Kramer, A. van der Laarse, A. V. Bruschke, and M. S. Feld, "Diagnosis of human coronary atherosclerosis by morphology-based Raman spectroscopy," Cardiovasc. Pathol. **10,** 59–68 (2001).

4. A. S. Haka, K. E. Shafer-Peltier, M. Fitzmaurice, J. Crowe, R. R. Dasari, and M. S. Feld, "Identifying microcalcifications in benign and malignant breast lesions by probing differences in their chemical composition using Raman spectroscopy," Cancer Res. **62,** 5375–5380 (2002).
5. R. Manoharan, K. Shafer, L. Perelman, J. Wu, K. Chen, G. Deinum, M. Fitzmaurice, J. Myles, J. Crowe, R. Dasari, and M. Feld, "Raman spectroscopy and fluorescence photon migration for breast cancer diagnosis and imaging," Photochem. Photobiol. **67,** 15–22 (1998).
6. T. J. Römer, J. F. B. Brennan, M. Fitzmaurice, M. L. Feldstein, G. Deinum, J. L. Myles, J. R. Kramer, R. S. Lees, and M. S. Feld, "Histopathology of human coronary atherosclerosis by quantifying its chemical composition with Raman spectroscopy," Circulation **97,** 878–885 (1998).
7. P. Libby, "Molecular bases of the acute coronary syndromes," Circulation **91,** 2844–2850 (1995).
8. J. M. Mann and M. J. Davies, "Vulnerable plaque: relation of characteristics to degree of stenosis in human coronary arteries," Circulation **94,** 928–931 (1996).
9. M. Shim and B. Wilson, "Development of an *in vivo* Raman spectroscopic system for diagnostic applications," J. Raman Spectrosc. **28,** 131–142 (1997).
10. M. Shim, B. Wilson, E. Marple, and M. Wach, "Study of fiber-optic probes for *in vivo* medical Raman spectroscopy," Appl. Spectrosc. **53,** 619–627 (1999).
11. J. Y. Ma and Y. S. Li, "Optical-fiber Raman probe with low-background interference by spatial optimization," Appl. Spectrosc. **48,** 1529–1531 (1994).
12. T. F. Cooney, H. T. Skinner, and S. M. Angel, "Comparative study of some fiber-optic remote Raman probe designs. 1. Model for liquids and transparent solids," Appl. Spectrosc. **50,** 836–848 (1996).
13. T. F. Cooney, H. T. Skinner, and S. M. Angel, "Comparative study of some fiber-optic remote Raman probe designs. 2. Tests of single-fiber, lensed, and flat- and bevel-tip multi-fiber probes," Appl. Spectrosc. **50,** 849–860 (1996).
14. U. Utzinger and R. Richards-Kortum, "Fiber optic probes for biomedical spectroscopy," J. Biomed. Opt. **8,** 121–147 (2003).
15. M. G. Shim, L.-M. W. K. Song, N. E. Marcon, and B. C. Wilson, "*In vivo* near-infrared Raman spectroscopy: demonstration of feasibility during clinical gastrointestinal endoscopy," Photochem. Photobiol. **72,** 146–150 (2000).
16. P. J. Caspers, G. W. Lucassen, R. Wolthuis, H. A. Bruining, and G. J. Puppels, "*In vitro* and *in vivo* Raman spectroscopy of human skin," Biospectroscopy **4,** S31–S39 (1998).
17. P. J. Caspers, G. W. Lucassen, H. A. Bruining, and G. J. Puppels, "Automated depth-scanning confocal Raman microspectrometer for rapid *in vivo* determination of water concentration profiles in human skin," J. Raman Spectrosc. **31,** 813–818 (2000).
18. T. R. Hata, T. A. Scholz, I. V. Ermakov, R. W. McClane, F. Khachik, W. Gellermann, and L. K. Pershing, "Non-invasive Raman spectroscopic detection of carotenoids in human skin," J. Invest. Dermatol. **115,** 441–448 (2000).
19. U. Utzinger, D. L. Heintzelman, A. Mahadevan-Jansen, A. Malpica, M. Follen, and R. Richards-Kortum, "Near-infrared Raman spectroscopy for *in vivo* detection of cervical precancers," Appl. Spectrosc. **55,** 955–959 (2001).
20. H. P. Buschman, E. T. Marple, M. L. Wach, B. Bennett, T. C. B. Schut, H. A. Bruining, A. V. Bruschke, A. van der Laarse, and G. J. Puppels, "*In vivo* determination of the molecular composition of artery wall by intravascular Raman spectroscopy," Anal. Chem. **72,** 3771–3775 (2000).
21. S. W. E. van de Poll, H. P. J. Buschman, M. J. Visser, J. H. van Bockel, A. van der Laarse, A. V. G. Bruschke, and G. J. Puppels, "Raman spectroscopy provides characterization of human atherosclerotic plaque composition *in vivo*," J. Am. Coll. Cardiol. **35,** 52A (2000).
22. G. Zhang, S. Demos, and R. Alfano, "Raman spectra of biomedical samples using optical fiber probes," in *Biomedical Sensing, Imaging, and Tracking Technologies II*, T. Vo-Dinh, R. Lieberman, and G. Vurek, eds., Proc. SPIE **2976,** 2–9 (1997).
23. G. Puppels, T. van Aken, R. Wolthuis, P. Caspers, T. Bakker Schutt, H. Bruining, T. Römer, H. Buschman, M. Wach, and J. Robinson, Jr., "*In vivo* tissue characterization by Raman spectroscopy," in *Infrared Spectroscopy: New Tool in Medicine*, H. Mantsch and M. Jackson, eds., Proc. SPIE **3257,** 78–83 (1998).
24. T. C. Bakker Schut, R. Wolthuis, P. J. Caspers, and G. J. Puppels, "Real-time tissue characterization on the basis of *in vivo* Raman spectra," J. Raman Spectrosc. **33,** 580–585 (2002).
25. M. Diem, *Introduction to Modern Vibrational Spectroscopy* (Wiley, New York, 1993).
26. R. L. McCreery, *Raman Spectroscopy for Chemical Analysis* (Wiley, New York, 2000).
27. R. W. Boyd, *Radiometry and the Detection of Optical Radiation* (Wiley, New York, 1983).
28. J. Ma and Y. S. Li, "Fiber Raman background study and its application in setting up optical fiber Raman probes," Appl. Opt. **35,** 2527–2533 (1996).
29. T.-W. Koo, "Measurement of blood analytes in turbid biological tissue using near-infrared Raman spectroscopy," Ph.D. dissertation (Massachusetts Institute of Technology, Cambridge, Mass., 2001).
30. J. M. C. van Gemert, R. M. Verdaasdonk, E. G. Stassen, G. A. C. M. Schets, G. H. M. Gijsbers, and J. J. Bonnier, "Optical properties of human blood vessel wall and plaque," Lasers Surg. Med. **5,** 235–237 (1985).
31. C. F. Bohren and D. R. Huffman, *Absorption and Scattering of Light by Small Particles* (Wiley, New York, 1983).
32. J. F. Brennan, Y. Wang, R. R. Dasari, and M. S. Feld, "Near-infrared Raman spectrometer systems for human tissue studies," Appl. Spectrosc. **51,** 201–208 (1997).
33. K. E. Shafer-Peltier, A. S. Haka, M. Fitzmaurice, J. Crowe, J. Myles, R. R. Dasari, and M. S. Feld, "Raman microspectroscopic model of human breast tissue: implications for breast cancer diagnosis *in vivo*," J. Raman Spectrosc. **33,** 552–563 (2002).
34. H. P. J. Buschman, G. Deinum, J. T. Motz, M. Fitzmaurice, J. R. Kramer, A. van der Laarse, A. V. G. Bruschke, and M. S. Feld, "Raman microspectroscopy of human coronary atherosclerosis: biochemical assessment of cellular and extracellular morphologic structures *in situ*," Cardiovasc. Pathol. **10,** 69–82 (2001).
35. T.-W. Koo, M. Hunter, A. M. K. Enejder, J. Oh, S. Sasic, R. R. Dasari, and M. S. Feld, George R. Harrison Spectroscopy Laboratory, Massachusetts Institute of Technology, 77 Massachusetts Avenue, Cambridge, Mass. 02139, are preparing a manuscript to be called "Development of a high sensitivity Raman spectroscopy system for biological studies."